PHYSICAL REVIEW B **93**, 014507 (2016)

Superconductivity pairing mechanism from cobalt impurity doping in FeSe: Spin ($s_{\pm}$) or orbital (s_{++}) fluctuation

T. Urata,[1] Y. Tanabe,[1,*] K. K. Huynh,[2] Y. Yamakawa,[3] H. Kontani,[3] and K. Tanigaki[1,2,†]
[1] *Department of Physics, Graduate School of Science, Tohoku University, Sendai 980-8578, Japan*
[2] *WPI—Advanced Institutes of Materials Research, Tohoku University, Sendai 980-8577, Japan*
[3] *Department of Physics, Nagoya University, Furo-cho, Nagoya 464-8602, Japan*

(Received 20 August 2015; revised manuscript received 10 November 2015; published 12 January 2016)

In high-superconducting transition temperature (T_c) iron-based superconductors, interband sign reversal ($s_{\pm}$) and sign preserving (s_{++}) s-wave superconducting states have been primarily discussed as the plausible superconducting mechanism. We study Co impurity scattering effects on the superconductivity in order to achieve an important clue on the pairing mechanism using single-crystal $\mathrm{Fe}_{1-x}\mathrm{Co}_x\mathrm{Se}$ and depict a phase diagram of a FeSe system. Both superconductivity and structural transition/orbital order are suppressed by the Co replacement on the Fe sites and disappear above $x = 0.036$. These correlated suppressions represent a common background physics behind these physical phenomena in the multiband Fermi surfaces of FeSe. By comparing experimental data and theories so far proposed, the suppression of T_c against the residual resistivity is shown to be much weaker than that predicted in the case of general sign reversal and full gap $s_{\pm}$ models. The origin of the superconducting paring in FeSe is discussed in terms of its multiband electronic structure.

DOI: 10.1103/PhysRevB.93.014507

I. INTRODUCTION

The superconducting paring mechanism of high-temperature superconductivity has been a long-lasting priority research area, and is one of the most important and intriguing scientific subjects. After discovery of Fe-based superconductors (FeSCs), the superconducting mechanism has been discussed from the viewpoint of their unique multiband Fermi surfaces. The superconducting gap functions primarily discussed in FeSCs are the interband sign reversal s-wave ($s_{\pm}$) and the sign preserving s-wave (s_{++}) states [1–3]. A stripe type antiferromagnetic spin fluctuation has been considered to mediate the $s_{\pm}$-wave state, while Fe $3d$ orbital fluctuation mediates the s_{++}-wave state.

Impurity scattering in superconductivity gives important information for understanding the pairing mechanism. A phonon mediated isotropic BCS superconductivity is robust against the nonmagnetic impurity scattering. Meanwhile, since the Cooper pair is glued by the k-dependent anisotropic scattering in the sign reversal superconductivity, e.g., (π,π) spin fluctuation in cuprates, similar impurities induce random scattering by ending up with a strong pair breaking [4,5]. A general theory of pair breaking in the latter case was given by Abrikosov and Gorkov (AG theory) [6]. In the FeSCs, impurities are expected to induce a significant reduction in superconducting transition temperature (T_c) for the $s_{\pm}$-wave states. Although the nonmagnetic impurity doping effects have been mostly examined by the AG theory in connection to the scaling relation between T_c and residual resistivity (ρ_0) [7–10], the important intrinsic multiband nature has been frequently neglected.

FeSe is one of the FeSC families showing superconductivity at around 9 K [11]. In the vicinity of the tetragonal/orthorhombic structural transition temperature ($T_s \approx$ 90 K), the orbital order has been recognized to develop without long-range antiferromagnetic (AFM) order, being in strong contrast with the other FeSCs [12–17]. A sign preserved superconducting state has been indicated by scanning tunneling microscopy (STM) and spectroscopy (STS) in single layer FeSe [18]. Nevertheless, in thicker films and bulk FeSe, the nodal superconducting gap has been suggested by STM and STS as well as the London penetration depth, implying the contribution of AFM spin fluctuation to the formation of the Cooper pairs [19,20]. Both neutron scattering and nuclear magnetic resonance have shown AFM spin fluctuations [16,17,21,22], whereas an imperfect nesting between electron and hole Fermi surfaces has been observed by orbital resolved angle-resolved photoemission spectroscopy (ARPES) [23]. Detailed studies on Co doping are considered to give an important hint for understanding the mechanism of superconductivity presently debated in FeSe.

In the present paper, we report systematic electrical transport studies on the effect of Co impurity doping for single-crystal FeSe. In the FeAs system, Co has been regarded as a nonmagnetic impurity and provides an additional electron as a carrier [24], being in contrast with the situation of Mn [25,26]. Present Hall coefficients and ARPES [27,28] support this understanding. Therefore, Co is considered to act as a nonmagnetic impurity and add an electron as an itinerant carrier to FeSe. Our present experimental data indicate a correlation between the suppression of T_c and that of the structural transition orbital order when Fe is replaced by Co. By carefully analyzing the dependencies between the suppression of T_c and ρ_0 and taking into consideration the realistic electron and hole Fermi surfaces in FeSe [29], we found that the suppression of T_c against ρ_0 is clearly weaker than that expected from both the AG theory and a recent more particular model for the $s_{\pm}$-wave state [30]. Our experimental observations give better agreement with the sign preserved superconducting gap states and suggest important multiorbital nature of Fermi surfaces for the occurrence in superconductivity of FeSe [3,31,32].

---

[*] Corresponding author: ytanabe@m.tohoku.ac.jp
[†] Corresponding author: tanigaki@sspns.phys.tohoku.ac.jp

II. EXPERIMENTS

High quality single crystals of $Fe_{1-x}Co_xSe$ ($0 \leqslant x \leqslant 0.075$) were grown by a molten salt flux method [14,33,34]. The temperature of hot and cold positions was kept at 390 and 240 °C, respectively. After ~10 days, single crystals were grown around the cold part of the quartz tube. Being different from the conventional method, polycrystalline samples [35] were employed as a precursor. Note that x_{nom} indicates the nominal composition of Co applied for synthesis of polycrystals. We examined the quality of the prepared samples by x-ray diffraction (XRD, Cu K-α radiation wavelength of 1.5406 Å) around the c axis as well as energy dispersive x-ray spectroscopy (EDS). The magnetic susceptibility was measured at $B = 1$T parallel to the ab plane. The temperature dependence of electrical resistivity and Hall resistance was measured by a four probe method. The superconducting transition temperatures (T_cs) were determined at the end point of the superconducting transition with a value of approximately less than 1.0×10^{-8} Ω cm. In the Hall resistance measurements, magnetic fields were varied in a range of $|B| \leqslant 9$ T parallel to the c axis.

III. RESULTS

A. Sample characterization

Figure 1(a) shows XRD spectra obtained for $x_{\mathrm{nom}} = 0$, 0.01, 0.025, 0.05, and 0.10. Clear $(00l)$ ($l = 1$–4) peaks were observed. No impurity peaks were detected within the experimental errors. Since the lattice shrinkage is very small in the case of Co doping [35], it was difficult to see a significant influence on their lattice parameters among samples with small concentration of Co even though the shift in the (004) peak between $x_{\mathrm{nom}} = 0$ and 0.10 was detected. The black squares in Fig. 1(b) represent the dependence of x_{nom} as a function of Co concentration determined by EDS (x_{EDS}). EDS spectra were taken at ten different positions on each specimen. The error bars were estimated as the standard deviations from the average. A monotonic increase in x_{EDS} was observed against x_{nom}. Note that the nominal concentration of $x_{\mathrm{nom}} = 0.01$ is used for the sample instead of x_{EDS} because EDS was not sufficiently sensitive for detecting the Co peak under such a small concentration. The blue circles in Fig. 1(b) show that the T_{kink} (the kink temperature in the resistivity curve as shown in the section of the electrical resistivity) reduced monotonically with x_{nom}. These experimental data indicate that the systematic substitution of Co was successfully accomplished. We regard x_{EDS} as the real x and used this for discussion hereafter. In the parent FeSe grown by a $KCl/AlCl_3$ flux method, no interstitial Fe was found by x-ray-diffraction measurements [33]. In order to check the interstitial Fe carefully in $Fe_{1-x}Co_xSe$, the concentration ratio (Fe+Co)/Se was compared against the nominal Co concentrations as shown in Fig. 1(c). Since the ratio is almost constant within the error bars for all nominal concentrations, the interstitial Fe is not influenced by the Co doping. It should be emphasized that we selected the samples with (Fe+Co)/Se < 1.05 for electrical transport measurements.

B. Electrical resistivity

Temperature dependence of the normalized electrical resistivity ($\rho/\rho_{300\mathrm{K}}$) for $Fe_{1-x}Co_xSe$ ($0 \leqslant x \leqslant 0.075$) is shown in Fig. 2(a). In parent FeSe, the $\rho/\rho_{300\mathrm{K}}$ showed a kink (T_{kink}) due to the structural transition [11,33]. This can clearly be seen as a dip of the first derivative as shown in Fig. 2(b). T_{kink} decreased with an increase in Co concentration and finally disappeared at $x = 0.036$, indicating that the high-temperature tetragonal phase holds above $x = 0.036$. As seen in the magnified ρ-T plots [Fig. 2(c)] at low temperatures, the T_c decreases with an increase in Co and the superconductivity is killed at $x = 0.036$ above 2 K. Both suppression of superconductivity and structural transition in FeSe occur by partial replacement of Fe with Co. In order to interpret the T_c suppression by Co in terms of the impurity scattering, residual resistivity ρ_0 was evaluated. The absolute values of resistivity (ρ) as a function of temperature are very sensitive to the measurement conditions and generally contain large errors arising from sample shape or/and inhomogeneity, etc. In order to estimate a reliable value, resistivity measurements were carefully performed on more than 20 samples selected from the same sample batch of $x_{\mathrm{nom}} = 0.025$. Figure 2(d) shows the results by excluding the samples showing large deviation from the average. Just above the T_cs, ρ of $x_{\mathrm{nom}} = 0.025$ ($x \approx 0.018$) are clearly larger than those of FeSe.

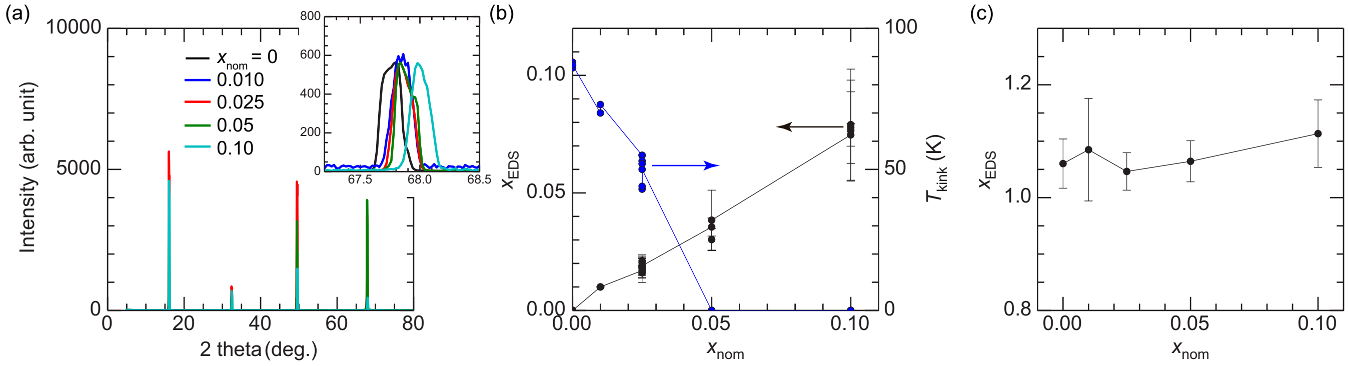

FIG. 1. (a) The x-ray-diffraction data of $Fe_{1-x}Co_xSe$ ($x_{\mathrm{nom}} = 0$, 0.010, 0.025, 0.05, and 0.10) around the c axis. The inset represents the normalized (004) peaks. (b) The nominal concentration (x_{nom}) dependence determined by EDS (x_{EDS}) and T_{kink}. T_{kink} is defined as the temperature showing a kink in the resistivity curve as described in the later section. (c) The nominal concentration dependence of concentration Fe+Co with respect to Se, i.e., (Fe+Co)/Se. The error bars are defined as the standard deviations of measurements.

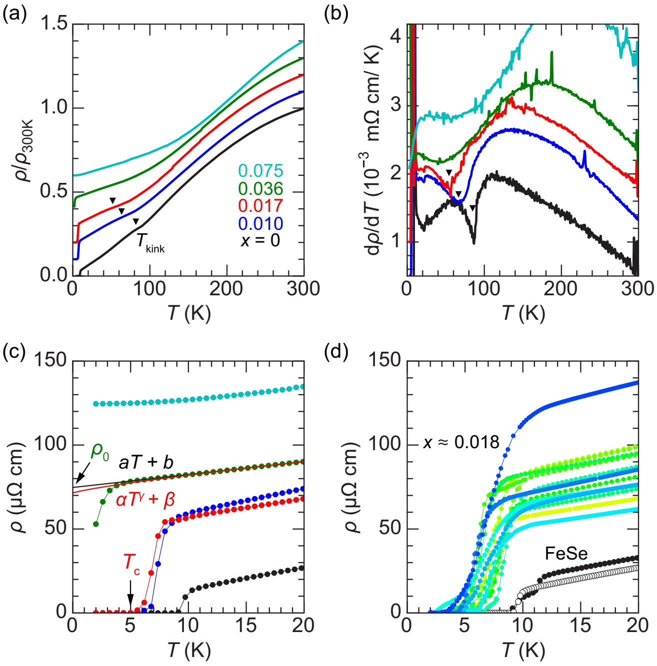

FIG. 2. (a) Normalized temperature dependence of resistivity ($\rho/\rho_{300\mathrm{K}}$). Note that each curve is shifted by 0.1 for clarity. The closed triangles indicate the kink in the resistivity curve (T_{kink}). T_{kink} is defined as the peak position of the first T derivative of ρ. (b) Temperature dependence of the first derivative of ρ. (c,d) Enlarged view of the temperature dependence of ρ. The curve is not shifted. (c) The black and the red lines show fitting results of ρ-T curves in the normal states using $\rho = (aT + b)$ or $(\alpha T^{\gamma} + \beta)$, respectively. (d) Closed and open black circles represent $x = 0$. The others (blue, yellow, and green) indicate $x_{\mathrm{nom}} = 0.025$. Their averaged concentration was $x \approx 0.018$.

In order to deduce residual resistivity (ρ_0), two types of fitting were employed. One is linear fitting using a function of $aT + b$, where b represents ρ_0. The other is fitting using a power function of $\alpha T^{\gamma} + \beta$, where β represents ρ_0. The fitting was made in the temperature range of 12–13 K (just above the superconducting onsets) to 25–27 K. An example of the fitting line is shown in Fig. 2(c). Figure 3 shows the x dependence of these fitting parameters. Although some errors can be recognized, ρ_0 apparently increases monotonically with x as seen in Fig. 3(a). The value of ρ_0 was not significantly affected by the fitting functions. The exponent γ in the power function is depicted against x in Fig. 3(b). At small concentrations it slightly decreases from ∼1.1 to ∼0.8 with x, and then jumps to $\gamma \approx 2.0$ at $x \approx 0.08$.

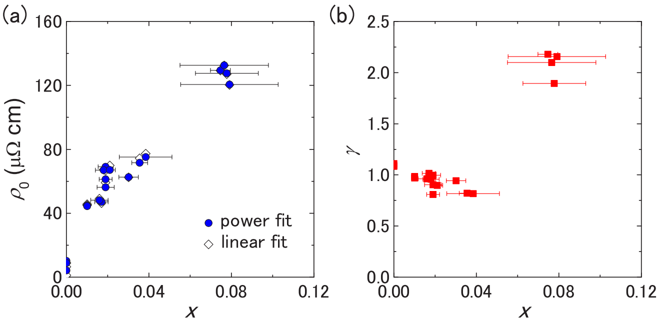

FIG. 3. (a) Co concentration (x) dependence of the residual resistivity, i.e., b in the $aT + b$ and β in the $\alpha T^{\gamma} + \beta$, vs x. (b) The exponent γ vs x.

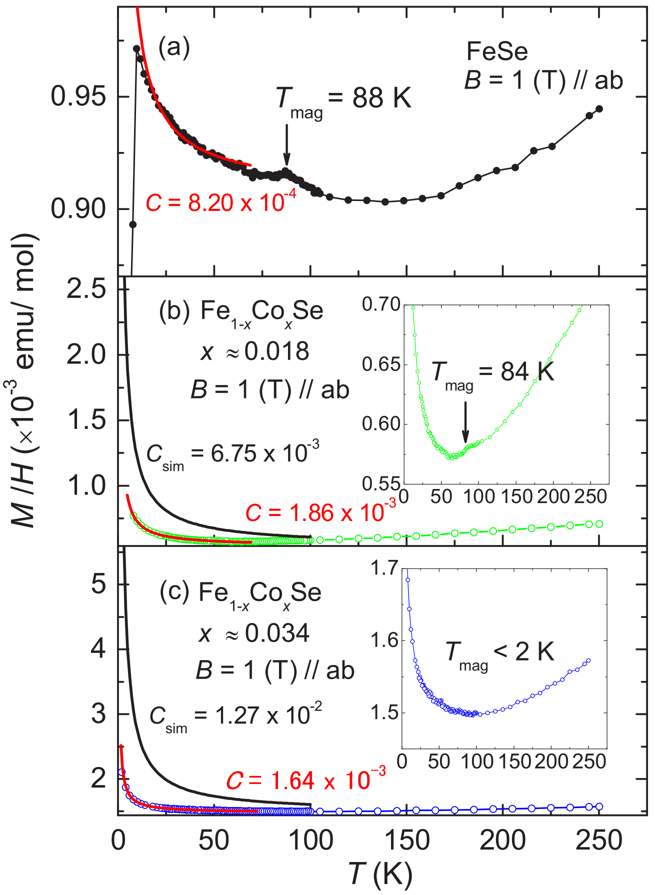

FIG. 4. Temperature dependence of magnetic susceptibility (M/H) for $\mathrm{Fe}_{1-x}\mathrm{Co}_x\mathrm{Se}$ with (a–c) $x \approx 0, 0.018, 0.034$. (b,c) Enlarged views are inserted. $B = 1$ T was applied in parallel to the ab plane of crystals. All data were taken on field cooling. The T_{mag} is defined as the kink of the curves. The red lines indicate Curie-Weiss fitting at low temperature, i.e., $C/T + A$ where C and A are the Curie constant and a certain real valued constant, respectively. The black lines also represent the Curie-Weiss curves with C_{sim} simulated by assuming that Co is a magnetic impurity with the angular momentum quantum number $J = 1/2$.

C. Magnetic susceptibility

Temperature dependence of magnetic susceptibility (M/H) was measured on field cooling for $\mathrm{Fe}_{1-x}\mathrm{Co}_x\mathrm{Se}$ ($x \approx 0, 0.018$, and 0.034) as shown in Fig. 4. A kink was observed in the temperature dependence of the M/H curve at the structural transition temperature in FeSe, being consistent with the earlier study [33]. We express this temperature as T_{mag} in the present paper. The T_{mag}, the transition temperature in spin magnetic moments, was also found in our samples of $x \approx 0$ and 0.018, but it disappears in the sample of $x \approx 0.034$. This disappearance, most presumably corresponding to the absence of the tetragonal to orthorhombic structural transition, coincides with the disappearance of T_{kink} and T^{*}.

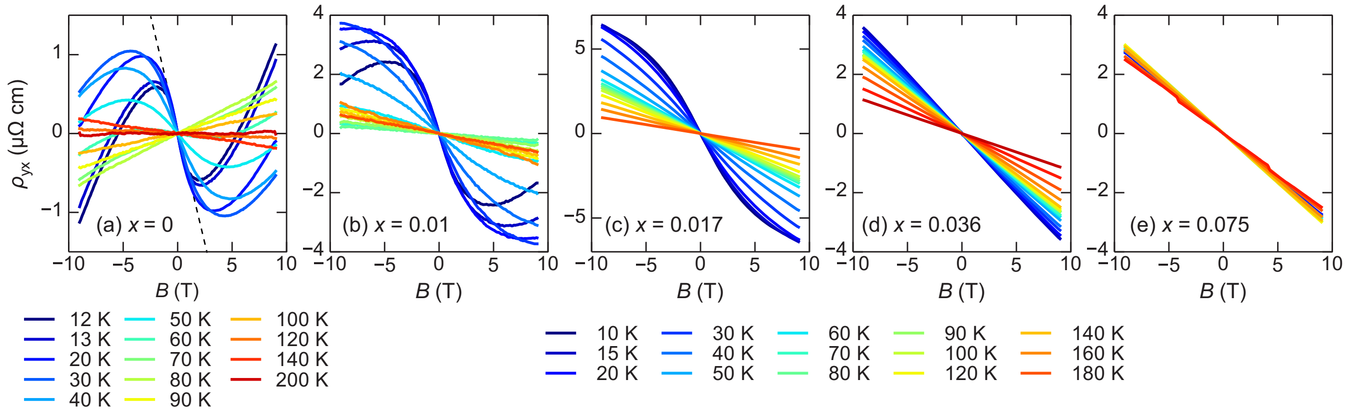

FIG. 5. Magnetic field (B) dependence of Hall resistivity (ρ_{yx}) of $x = 0$, 0.010, 0.017, 0.036, and 0.075 [(a)–(e), respectively]. The linear fitting line to derive the Hall coefficient (R_H) in the low B limit is shown as a dashed line in (a). The ρ_{yx}s were measured at different temperatures for $x = 0$ as noted in the legend at bottom left.

In order to confirm the magnetic statement of Co, M/H curves were fitted in a low-temperature range (15–60 K) by a function $C/T + A$, where the Curie constant is assumed to be C and A is a certain constant value. As shown in Fig. 4, the fitting curves are represented as red lines and the obtained C merely changes as a small value with an increase in x. For comparison, the Curie constants were simulated (C_{sim}) by assuming that all Co elements are localized with spin 1/2. The evaluated black curves show large deviations from the experimental plots. The obtained values of the Curie constant were much smaller than the doped cobalt concentration and did not change significantly. This result supports the scenario that the cobalt is acting as a nonmagnetic impurity in the $Fe_{1-x}Co_xSe$ system.

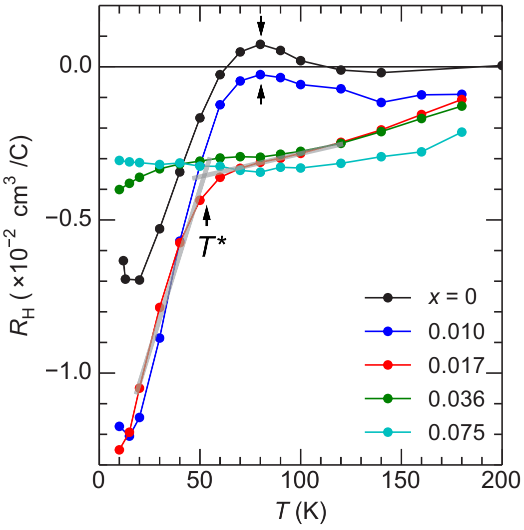

FIG. 6. Temperature dependence of Hall coefficient (R_H) estimated in the low magnetic field regime. The black arrows indite the temperature where R_H starts suddenly decreasing (T^*). For $x = 0.017$, T^* is defined as the intersection point of two linear fitting lines shown as gray in color.

D. Hall resistivity

The magnetic field (B) dependence of Hall resistivity (ρ_{yx}) is shown in Fig. 5. In order to remove the extrinsic deviations from symmetric components caused by the misalignment of electrodes, corrections were made on the raw ρ_{yx} curves:

$$\rho_{yx}(+|B|) = \frac{\rho_{yx}^{\text{raw}}(+|B|) - \rho_{yx}^{\text{raw}}(-|B|)}{2}. \tag{1}$$

A strong nonlinear behavior at low temperatures was moderated as x increases. This can be understood to be caused by the suppression of mobility. Moreover, temperature dependence was also moderated, being consistent with the Hall coefficient (R_H) T dependence described later. R_H was determined from the slope of ρ_{yx} at low B where ρ_{yx}s develop linearly. The linear fitting is displayed as a dashed line in Fig. 5(a).

Temperature dependence of R_H is shown in Fig. 6. For the parent FeSe, R_H became positive at around T_{kink} and dropped with decreasing temperature. We define T^* as the temperature where R_H shows a sudden decrease. For $x = 0.017$, T^* is derived from the intersection of two linear fitting lines as shown in the gray lines of Fig. 6. With an increase in Co concentration, T^* lowered and almost disappeared at $x = 0.036$, being consistent with the disappearance of T_{kink}. The amplitude of R_H at low temperatures once increased and then decreased with an increase in x. When the concentration of Co exceeds $x = 0.036$, the observed change in R_H is nearly suppressed.

IV. ANALYSES OF T_c SUPPRESSION RATE BY CO DOPING

Figure 7 shows the x dependence of T_c. T_c monotonically decreased with an increase in x within the experimental errors. Figure 8 represents the T_c as a function of ρ_0. The ρ_0 values were estimated from the intercepts of the linear fitting (white diamonds) and the T^γ fitting (blue circles) on the resistivity curves at low temperatures as shown in Fig. 2(c). T_c monotonically decreased with an increase in ρ_0 and disappeared at ρ_0 of ≈60–80 $\mu\Omega$ cm.

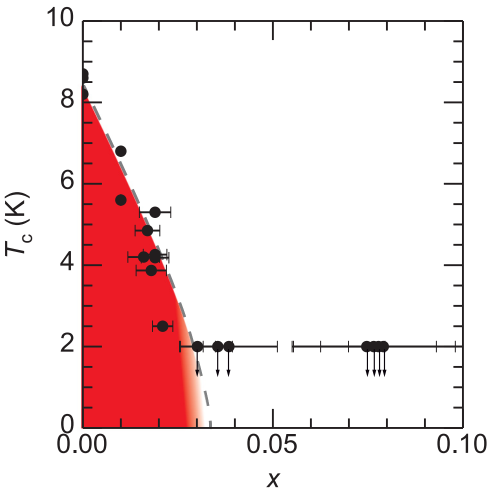

FIG. 7. The Co concentration (x) dependence of the superconducting transition temperature (T_c). Down arrows indicate that the zero resistivity is not observed above 2 K. The gray broken line is a guide to the eye.

A. AG theory in realistic two-band model

In order to clarify the superconducting pairing mechanism in FeSe, here we evaluate how T_c is suppressed against residual resistivity when Co is doped as an impurity in the light of two models. The first model is the AG theory, which can be applicable to the sign reversal superconducting states [6]. The other is the specific model formulated for the full gap $s_\pm$-wave states theoretically calculated based on the realistic physical condition of FeSCs [30]. Both models are valid in the limit that nonmagnetic impurities are not incorporated to a great extent. The AG theory is formulated as

$$\ln\left(\frac{T_c^{AG}}{T_c^0}\right) = \Psi\left(\frac{1}{2}\right) - \Psi\left(\frac{1}{2} + \frac{\hbar}{4\pi\tau k_B T_c^{AG}}\right), \tag{2}$$

where k_B is the Boltzmann constant, T_c^0 is the superconducting transition temperature in the pristine material, τ is the scattering time, and $\Psi(z)$ is the digamma function. Here we use superconducting transition temperature as T_c^{AG} to differentiate from experimental values (T_c). The pair breaking energy is characterized by τ. The value of τ was computed at each value of T_c^{AG} using Eq. (2) with $T_{c0} = 9$ K. In order to compare the AG theory and our experimental data, τ needs to be converted into the residual resistivity in a reasonable way as follows.

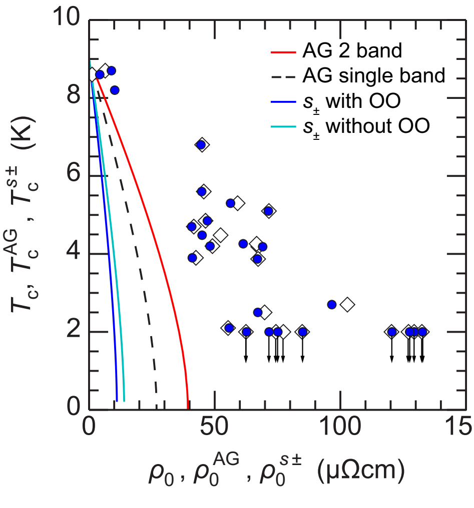

FIG. 8. Dependence of the superconducting transition temperature (T_c) on the residual resistivity (ρ_0). The ρ_0 was estimated by fitting ρ-T curves in the normal states as shown in Fig. 2(c). White diamonds and blue circles represent ρ_0 estimated by T-linear and T^γ type fitting functions, respectively. With realistic band parameters, the red, blue, and cyan lines are drawn by the AG theory (T_c^{AG} vs ρ_0^{AG}) and the $s_\pm$-wave model ($T_c^{s\pm}$ vs $\rho_0^{s\pm}$) with and without orbital order (OO), respectively. The dashed line represents the AG theory in the conventional single carrier model.

In FeSe, nearly semimetallic electronic structure is realized [14,15,20,34,36]. The ARPES reported a single electron Fermi surface (FS) around the M point and a single hole FS around Γ. It should be mentioned that the recent mobility spectrum analysis and the quantum oscillation measurements in magnetoresistance reported an additional small FS [34,37]. In the present work, since an influence of this tiny FS may be small in the present analysis, we focus on the two main FSs observed by ARPES. In this system, therefore, conductivity can be described in a nearly free-electron model by keeping the effective mass (m^*) constant on each FS as follows:

$$\sigma = \eta_1 e^2 \tau_1 + \eta_2 e^2 \tau_2, \tag{3}$$

where $\eta_i = n_i/m_i^*(i{=}1{,}2)$ and n_i is a carrier density of ith FS. From this equation we define a weighted average τ (τ_{ave}) as

$$\tau_{ave} = \frac{\eta_1\tau_1 + \eta_2\tau_2}{\eta_1 + \eta_2}. \tag{4}$$

Therefore,

$$\sigma = (\eta_1 + \eta_2)e^2\tau_{ave}. \tag{5}$$

Thus, the relation between the residual resistivity ($\rho_0^{AG} \equiv 1/\sigma$) and τ_{ave}, which should correspond to the τ in Eq. (2), is derived. The information on FeSe achieved from the ARPES measured at 30 K to calculate η_i is shown in Table I [14,29]. Since the anisotropy of the hole FS at Γ is smaller than the electron FS at the M point, the observed ARPES may represent such an averaged value. For each FS, m^* was calculated by the relation $m^* = \hbar^2 k_F/v_F^{ave}$. The v_F was averaged over the electron FS and was evaluated as v_F^{ave}. The general carrier density definition is

$$n = \frac{2}{(2\pi)^3}\int_{k\leqslant k_F} dk^3, \tag{6}$$

where the factor of 2 is for the spin degeneracy and the integration is performed for the entire volume surrounded by

TABLE I. Results of the ARPES measurements at 30 K [14,29]. Note that several photon energy results are averaged.

	Γ	M (long axis)	M (short axis)
k_F (Å^{-1})	0.11	0.20	0.05
v_F (eV Å)	0.18	0.50	0.20

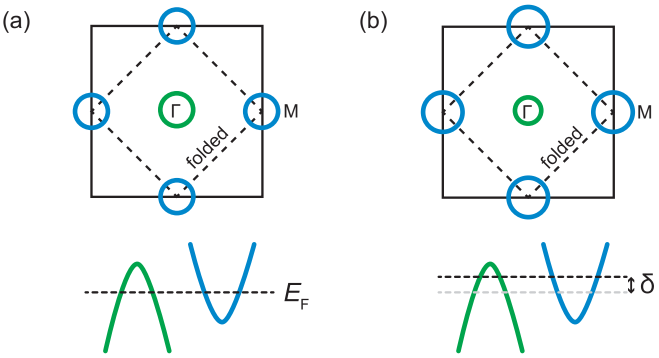

FIG. 9. A schematic view of Fermi surfaces of (a) the two-band semimetallic structure and (b) the electron doped one on the k_x-k_y plane. The bottom figure represents the rigid band Fermi-energy shift due to the electron doping by δ.

the FS. Given the elliptic cylinder, n can be calculated as

$$n = \frac{k_F^l k_F^s}{2\pi c}, \tag{7}$$

where k_F^l and k_F^s denote the Fermi wave number of the longer and the shorter axes of the ellipse, respectively. The c-axis cell parameter expressed as c in the real space is taken from literature [38]. Now we can calculate the ρ_0^{AG} in the framework of nearly free-electron approximation from Eq. (5). The obtained parameters are $n_1 \approx 2.90 \times 10^{26}$ m^{-3}, $n_2 \approx 3.35 \times 10^{26}$ m^{-3} and $m_1^* \approx 2.28 \times 10^{-30}$ kg, $m_2^* \approx 4.26 \times 10^{-30}$ kg, where the indices of 1 and 2 represent the electron and the hole bands, respectively.

The obtained dependence, i.e., T_c^{AG} versus ρ_0^{AG}, is represented by a solid red line in Fig. 8. The suppression of T_c^{AG} is clearly faster than our experimental data. Given a conventional single-band model, for comparison, the analytical expectation (dashed line) is represented in the same figure, where the carrier number n was evaluated from R_H data measured at low B. The averaged effective mass was employed to calculate ρ_0^{AG}. The suppression of T_c^{AG} is faster in the single-band model than in the two-band model. Since the amplitude of R_H is suppressed in a compensated semimetallic state, the single-band model ($R_H = 1/ne$) overestimates n and consequently leads to faster suppression of T_c^{AG}.

1. Electron doping effects on the two-band model

We interpret the electron doping effects on our fitting model based on a nearly free-electron model. If the carrier doping rigidly shifts the Fermi energy (E_F) as represented in Fig. 9, the conductivity is shown not to be affected by $\eta_1 + \eta_2$ but determined only by τ_{ave} as follows: In a nearly free-electron model, the energy dispersion relation of an electron band is written as

$$E(\mathbf{k}) = \frac{\hbar^2|\mathbf{k}|^2}{2m^*} - E_F. \tag{8}$$

The amplitude of the Fermi wave number is derived by setting $E(\mathbf{k}) = 0$ as $|\mathbf{k}_F| = \pm\sqrt{2m^* E_F}/\hbar$. The carrier density of a two-dimensional FS (a cylinder) is

$$n = \frac{|\mathbf{k}_F|^2}{2\pi c} = \frac{m^* E_F}{\pi \hbar^2 c}. \tag{9}$$

By assuming electron doping by δ, E_F becomes $E_F + \delta$. The value of m^* is not modified in a rigid band model. Therefore the conductivity after the electron doping can be written as

$$\begin{aligned} \sigma &= (\eta_1' + \eta_2')e^2\tau_{ave}' \\ &= \left(\frac{E_F^{(1)} + \delta}{\pi\hbar^2 c} + \frac{E_F^{(2)} - \delta}{\pi\hbar^2 c}\right)e^2\tau_{ave}' \\ &= (\eta_1 + \eta_2)e^2\tau_{ave}', \end{aligned} \tag{10}$$

where $E_F^{(1)}$ and $E_F^{(2)}$ represent the Fermi energy of electron and hole bands, respectively. Therefore, $(\eta_1 + \eta_2)$ of a two-dimensional nearly free-electron model does not change by rigid band shift. As long as the approximation is valid, the effect of Co substitution can be simplified to the scattering time problem.

B. Theory of impurity-induced reduction in T_c for the full gap $s_\pm$-wave state

The second model to analyze the suppression of T_c is a realistic multiorbital theory. Here, we employed a multiorbital tight-binding model for FeSe with realistic Fermi surfaces in order to perform quantitative theoretical studies of the impurity effect on the $s_\pm$-wave state. The following two theoretical models are introduced: In model (a), the orbital order is absent and the C_4 symmetry is preserved. In model (b), the experimentally observed sign reversing orbital polarization is introduced, by which the symmetry is lowered to C_2. The Fermi surfaces of these models without carrier doping are shown in Figs. 10(a) and 10(b), respectively. The carrier numbers per Fe site are $n_h = 2.02\%$ and $n_e = 2.02\%$ in model (a) and $n_h = 1.95\%$ and $n_e = 1.94\%$ in model (b). In model (a) [model (b)], the hole pockets disappear by introducing 3.0% (3.7%) electron carriers induced by Co doping. This result would be consistent with the disappearance of the structure transition by 3.6% Co doping as observed experimentally.

In order to construct the model (a) without the orbital order, we first performed LDA band calculations for FeSe using the WIEN2K package, and made the tight-binding fitting using the WIEN2WANNIER package. However, the obtained Fermi pockets are too large. To reproduce the tiny Fermi pockets experimentally observed in FeSe, we introduced the orbital-dependent energy shifts at Γ, $X(Y)$, and M points ($\delta E_\Gamma, \delta E_X, \delta E_M$): We set $(\delta E_\Gamma, \delta E_{X,Y}, \delta E_M) = (-0.26, 0.13, 0)$ for xz and yz orbitals and $(\delta E_\Gamma, \delta E_{X,Y}, \delta E_M) = (0, 0.26, -0.25)$ for xy orbitals in units of eV. Such level shifts were introduced by the additional intraorbital hopping integrals: $\delta t^{\rm onsite} = \delta E_\Gamma/4 + \delta E_{X,Y}/2 + \delta E_M/4$, $\delta t^{\rm nn} = \delta E_\Gamma/8 - \delta E_{X,Y}/8$, and $\delta t^{\rm nnn} = \delta E_\Gamma/16 + \delta E_{X,Y}/16 - \delta E_M/8$. In the model (b), we further introduced orbital polarization with sign reversal: $E_{yz} - E_{xz} = -0.02$ eV at Γ and M points and $E_{yz} - E_{xz} = 0.02$ eV at X and Y points.

Figure 10(c) shows the impurity-induced reduction in T_c of the $s_\pm$-wave state for $T_{c0} = 9$ K as a function of residual resistivity ρ_0, obtained by applying the T-matrix approximation. We used the realistic first-principles impurity potential model

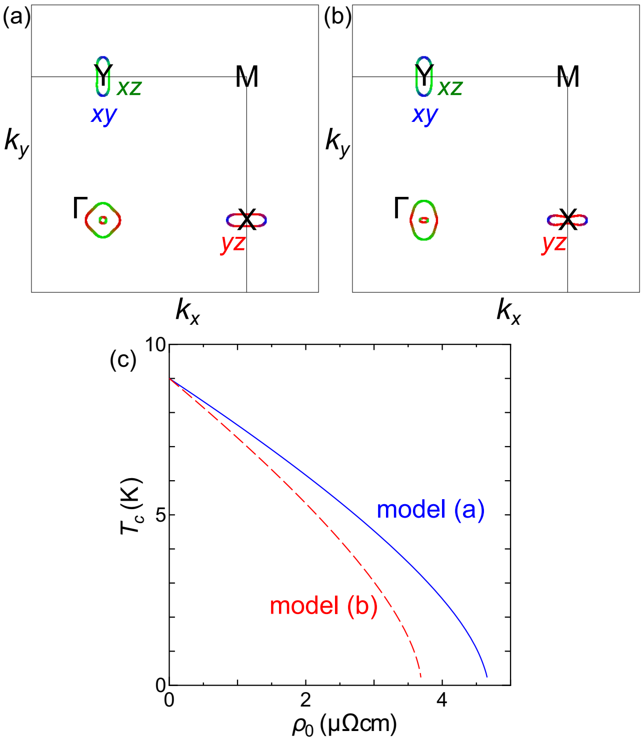

FIG. 10. Fermi surfaces of the present tight-binding models for FeSe (a) without orbital polarization and (b) with orbital polarization with sign reversal between Γ and $X(Y)$ points. (c) Obtained impurity-induced reduction in T_c for the $s_\pm$-wave state as a function of residual resistivity ρ_0 ($T_c = 9$ K), in both models (a) and (b).

for the Co ion given in [39], and neglected the carrier doping effect by Co doping. Here, we introduced the effective intraorbital and interpocket repulsive pairing interactions due to the spin fluctuations, by adjusting the strength to realize $T_{c0} = 9$ K. The detailed explanations for the gap equation analysis had been given in [30]. In the spin-fluctuation pairing mechanism in FeSe, only the electrons with xz and yz orbital characters contribute to the superconductivity since the xy orbital is absent in the hole pocket [40]. We also put the renormalization for the xz and yz orbitals (z) to be unity. In both models (a) and (b), the superconducting state disappears when the residual resistivity is $\rho_0^{\mathrm{cr}} \approx 4[\mu\Omega\,\mathrm{cm}]$, insensitively to the orbital polarization. The current vertex correction for ρ_0 was taken into account, and ρ_0 was kept independent of z. If the experimental value $z \approx 1/3$ for the xz and yz orbitals is taken into account [41], the critical residual resistivity is multiplied by z^{-1}. Therefore, $\rho_0^{\mathrm{cr}} \approx z^{-1}4[\mu\Omega\,\mathrm{cm}]$. Note that the total carrier number n_{carrier} is ∼4% per Fe ion in both model (a) and model (b). In a model with $n_{\mathrm{carrier}} \sim 2.5\%$ by reducing the sizes of Fermi pockets, the relation $\rho_0^{\mathrm{cr}} \approx z^{-1}6.5[\mu\Omega\,\mathrm{cm}]$ is realized.

Based on the $\rho_0^{\mathrm{cr}} \approx z^{-1}4[\mu\Omega\,\mathrm{cm}]$ with $z^{-1} \sim 3$, the superconducting transition temperature ($T_c^{s\pm}$) suppression predicted in the $s_\pm$-wave state is displayed by the blue (the orbital order is considered) and cyan (the orbital order is not considered) lines in Fig. 8. In both cases, the calculated results show faster reductions of $T_c^{s\pm}$ than the experimental data, being consistent with that in the first model.

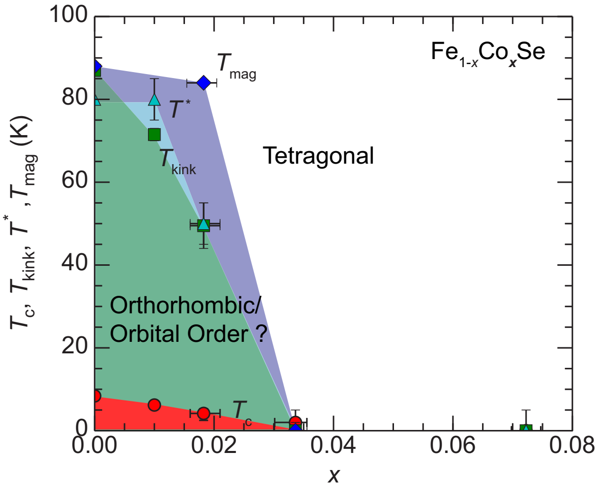

FIG. 11. An electronic phase diagram of $\mathrm{Fe}_{1-x}\mathrm{Co}_x\mathrm{Se}$. The superconducting transition temperature (T_c : red circles), the temperature showing a kink in the ρ-T curve (T_{kink}: green squares), and the temperature showing a sudden decrease in the Hall coefficient (T^*: light blue triangles) are represented. T_{mag} (blue diamonds) represents a kink observed in temperature dependence of magnetic susceptibility.

V. DISCUSSION

A. Electronic phase diagram

The experimental observations in $\mathrm{Fe}_{1-x}\mathrm{Co}_x\mathrm{Se}$ are summarized in a phase diagram shown in Fig. 11. The R_{H} at low temperatures increases first and then decreases with an increase in x of Co as shown in Fig. 6. Above $x = 0.036$, R_{H} becomes nearly constant against x. In a two-band semiclassical model, the low-field limit of the Hall coefficient can be written as

$$R_{\mathrm{H}} = \frac{p\nu^2 - n\mu^2}{e(p\nu + n\mu)^2}, \tag{11}$$

where n, p and μ, ν are the carrier concentrations and the mobilities of holes and electrons, respectively. ARPES, STM, and transport studies have demonstrated that the electronic structure in the orthorhombic FeSe is almost compensated semimetal [14,15,20,34]. In a compensated semimetal ($n \approx p$), the amplitude of R_{H} is suppressed due to the electron and hole compensation as shown in Eq. (11). When electrons are doped to FeSe, the compensation breaks to increase the amplitude of R_{H}. Further electron doping may shrink and vanish the tiny hole pocket. In such a case, since a single carrier picture is more appropriate, the amplitude of R_{H} is suppressed. Therefore, our experimental observations on the Co doping dependence R_{H} in $\mathrm{Fe}_{1-x}\mathrm{Co}_x\mathrm{Se}$ can qualitatively be understood in terms of the electron doping by Co. For $x = 0.036$ and 0.075, where the high-temperature tetragonal phase remains in an entire temperature range, the R_{H} at 10 K gives the carrier number (n) of $\sim 10^{21}\ \mathrm{cm}^{-3}$ in a single carrier model (i.e., $R_{\mathrm{H}} = 1/n$). By assuming the rigid band shift of the Fermi energy in $\mathrm{Fe}_{1-x}\mathrm{Co}_x\mathrm{Se}$, the carrier number in the electron pocket above $x = 0.036$ is deduced to be $\sim 10^{21}\ \mathrm{cm}^{-3}$ based on the carrier numbers of the electron and the hole pockets in FeSe [34], being comparable with those in $x = 0.036$ and 0.075. Since the variation observed in R_{H} is consistent with the electron doping provided by Co, potential scattering and changes in both the type and the number of carriers influence the phase diagram in Fig. 11. Note that quantitative analysis centering on the Hall resistivity curvature is not realistic in the present magnetic field regime. The transverse magnetoresistance is ≈10% at $T = 10$ K and $B = 9$ T for $x \approx 0.018$ whereas it is ≈300% in the parent FeSe [34], suggesting the significant suppression in carrier mobility by the Co scattering effects. Since only a limited number of carriers contribute to the magnetotransport below 9 T, any reasonable analysis on the magnetotransport data would not accurately be valid [42,43]. Semiclassical multicarrier fitting of Hall resistivity assuming the number of electron and hole pockets could not give correct transport parameters for anisotropic Fermi surfaces, and somewhat more sophisticated analyses such as a mobility spectrum method are necessary [34]. For preventing these uncertain factors in discussion, we employed the band parameters extracted from the ARPES data for the present discussion.

Both superconductivity and structural transition are suppressed by Co doping and disappear at $x = 0.036$. This is consistent with the disappearance of the kink in magnetic susceptibility curves (T_{mag}). Since the orbital order was reported to develop in the orthorhombic phase of FeSe, the present results may also indicate the suppression to be correlated between superconductivity and orbital order by Co doping. Theoretically, nesting between electron and hole pockets is predicted to be important for both superconductivity and orbital order [1–3] in FeSCs [32,44,45]. In FeSe, electron doping may also suppress the nesting due to the small Fermi energies [20], being consistent with the experimentally observed evolution of the R_{H} as a function of x. Hence, the suppression correlated among superconductivity, structural phase transition, and orbital order may originate from the reduction in nesting between electron and hole pockets.

B. Paring mechanism

If the sign reversal superconducting mechanism could be dominant in FeSe, suppression in superconductivity would be similar to that predicted by both theories of AG and the full gap $s_{\pm}$-wave states. However, the suppression experimentally observed as T_c was much smaller than that described in these models. Consequently, the sign preserved superconducting mechanism will be more appropriate for $\mathrm{Fe}_{1-x}\mathrm{Co}_x\mathrm{Se}$. In FeSe, a nodal superconducting gap was experimentally observed in the electron pocket [20,46]. Meanwhile, orbital resolved ARPES demonstrated an imperfect antiferromagnetic nesting between the electron and the hole Fermi surfaces. One can imagine that the sign reversal and the sign preserved pairing mechanism may compete with each other via the inter- and the intraorbital scattering [1–3,32,45]. In this case, the sign preserved pairing mechanism may give a primary contribution in FeSe from the viewpoint of the T_c suppression observed in our experimental data. Another possible scenario may be that the superconducting gap structure changes from a nodal s- to an s_{++}-wave state. It has been pointed out that the node of the superconducting gap is not protected by symmetry, and an accidental node [20,47] was suggested. The superconducting gap may change from a nodal gap to a full gap state depending on the quality of single crystals. In such a case, the potential scattering induced by Co may lift the node to open a superconducting gap, resulting in a change of gap structure from the nodal- to the s_{++}-wave state. It should be noted that sign preserved superconducting gap structure has been proposed for single layered FeSe on SrTiO_3 [18] possessing highly electron doped band structure [48]. Our observations are consistent with these previous works.

VI. CONCLUSION

We investigated the nonmagnetic Co impurity doping effect on the superconductivity and the structural transition/orbital order in FeSe. In the electronic phase diagram of $\mathrm{Fe}_{1-x}\mathrm{Co}_x\mathrm{Se}$, both superconductivity and structural transition/orbital order were suppressed by Co doping and disappeared at $x = 0.036$. Experimental data of the T_c suppression against the residual resistivity were compared to the values expected from the AG theory [6] and a full gap $s_{\pm}$ theory [30]. Our data showed much slower suppression than that from both theories. As a result, the sign preserved superconducting mechanism is more appropriate to explain the superconducting pairing mechanism in FeSe. In FeSe, the interband Fermi surface nesting including both intra- and interorbital scattering processes plays an essential role for the superconducting pairing mechanism and for the normal state phase diagram [32,44,45]. The present studies unveiled a part of the complex electronic states. Considering the electronic structures taking place in this system, small perturbation may change the situation in a more complex manner in the $\mathrm{Fe} - 3d$ multiband system by changing one state to another.

ACKNOWLEDGMENTS

The authors are grateful to K. Nakayama for providing the unpublished angle-resolved photoemission spectroscopy results of $\mathrm{Fe}_{1-x}\mathrm{Co}_x\mathrm{Se}$ and fruitful discussions. T.U. was supported by the Research Fellowship of Japan Society for the Promotion of Science.

---

[1] I. I. Mazin, D. J. Singh, M. D. Johannes, and M. H. Du, Phys. Rev. Lett. **101**, 057003 (2008).

[2] K. Kuroki, S. Onari, R. Arita, H. Usui, Y. Tanaka, H. Kontani, and H. Aoki, Phys. Rev. Lett. **101**, 087004 (2008).

[3] H. Kontani and S. Onari, Phys. Rev. Lett. **104**, 157001 (2010).

[4] F. J. Ohkawa and H. Fukuyama, J. Phys. Soc. Jpn. **53**, 4344 (1984).

[5] K. Ishida, Y. Kitaoka, N. Ogata, T. Kamino, K. Asayama, J. Cooper, and N. Athanassopoulou, J. Phys. Soc. Jpn. **62**, 2803 (1993).

[6] A. A. Abrikosov and L. P. Gor'kov, Zh. Eksp. Teor. Fiz. **39**, 1781 (1960) [Sov. Phys. JETP **12**, 1243 (1961)].

[7] M. Sato, Y. Kobayashi, S. C. Lee, H. Takahashi, E. Satomi, and Y. Miura, J. Phys. Soc. Jpn. **79**, 014710 (2010).

[8] Y. Nakajima, T. Taen, Y. Tsuchiya, T. Tamegai, H. Kitamura, and T. Murakami, Phys. Rev. B **82**, 220504 (2010).

[9] K. Kirshenbaum, S. R. Saha, S. Ziemak, T. Drye, and J. Paglione, Phys. Rev. B **86**, 140505 (2012).

[10] T. Inabe, T. Kawamata, T. Noji, T. Adachi, and Y. Koike, J. Phys. Soc. Jpn. **82**, 044712 (2013).

[11] F.-C. Hsu, J.-Y. Luo, K.-W. Yeh, T.-K. Chen, T.-W. Huang, P. M. Wu, Y.-C. Lee, Y.-L. Huang, Y.-Y. Chu, D.-C. Yan, and M.-K. Wu, Proc. Natl. Acad. Sci. USA **105**, 14262 (2008).

[12] H. Kotegawa, S. Masaki, Y. Awai, H. Tou, Y. Mizuguchi, and Y. Takano, J. Phys. Soc. Jpn. **77**, 113703 (2008).

[13] T. M. McQueen, A. J. Williams, P. W. Stephens, J. Tao, Y. Zhu, V. Ksenofontov, F. Casper, C. Felser, and R. J. Cava, Phys. Rev. Lett. **103**, 057002 (2009).

[14] K. Nakayama, Y. Miyata, G. N. Phan, T. Sato, Y. Tanabe, T. Urata, K. Tanigaki, and T. Takahashi, Phys. Rev. Lett. **113**, 237001 (2014).

[15] T. Shimojima, Y. Suzuki, T. Sonobe, A. Nakamura, M. Sakano, J. Omachi, K. Yoshioka, M. Kuwata-Gonokami, K. Ono, H. Kumigashira, A. E. Böhmer, F. Hardy, T. Wolf, C. Meingast, H. v. Löhneysen, H. Ikeda, and K. Ishizaka, Phys. Rev. B **90**, 121111 (2014).

[16] S.-H. Baek, D. V. Efremov, J. M. Ok, J. S. Kim, J. van den Brink, and B. Büchner, Nat. Mater. **14**, 210 (2015).

[17] A. E. Böhmer, T. Arai, F. Hardy, T. Hattori, T. Iye, T. Wolf, H. v. Löhneysen, K. Ishida, and C. Meingast, Phys. Rev. Lett. **114**, 027001 (2015).

[18] Q. Fan, W. H. Zhang, X. Liu, Y. J. Yan, M. Q. Ren, R. Peng, H. C. Xu, B. P. Xie, J. P. Hu, T. Zhang, and D. L. Feng, Nat. Phys. **11**, 946 (2015).

[19] C.-L. Song, Y.-L. Wang, P. Cheng, Y.-P. Jiang, W. Li, T. Zhang, Z. Li, K. He, L. Wang, J.-F. Jia, H.-H. Hung, C. Wu, X. Ma, X. Chen, and Q.-K. Xue, Science **332**, 1410 (2011).

[20] S. Kasahara, T. Watashige, T. Hanaguri, Y. Kohsaka, T. Yamashita, Y. Shimoyama, Y. Mizukami, R. Endo, H. Ikeda, K. Aoyama, T. Terashima, S. Uji, T. Wolf, H. von Löhneysen, T. Shibauchi, and Y. Matsuda, Proc. Natl. Acad. Sci. USA **111**, 16309 (2014).

[21] M. C. Rahn, R. A. Ewings, S. J. Sedlmaier, S. J. Clarke, and A. T. Boothroyd, Phys. Rev. B **91**, 180501 (2015).

[22] Q. Wang, Y. Shen, B. Pan, Y. Hao, M. Ma, F. Zhou, P. Steffens, K. Schmalzl, T. R. Forrest, M. Abdel-Hafiez, D. A. Chareev, A. N. Vasiliev, P. Bourges, Y. Sidis, H. Cao, and J. Zhao, Nat. Mater., doi:10.1038/NMAT4492.

[23] Y. Suzuki, T. Shimojima, T. Sonobe, A. Nakamura, M. Sakano, H. Tsuji, J. Omachi, K. Yoshioka, M. Kuwata-Gonokami, T. Watashige, R. Kobayashi, S. Kasahara, T. Shibauchi, Y. Matsuda, Y. Yamakawa, H. Kontani, and K. Ishizaka, Phys. Rev. B **92**, 205117 (2015).

[24] Y. Sekiba, T. Sato, K. Nakayama, K. Terashima, P. Richard, J. H. Bowen, H. Ding, Y.-M. Xu, G. H. Cao, Z.-A. Xu, and T. Takahashi, New J. Phys. **11**, 025020 (2009).

[25] Y. Texier, Y. Laplace, P. Mendels, J. T. Park, G. Friemel, D. L. Sun, D. S. Inosov, C. T. Lin, and J. Bobroff, Europhys. Lett. **99**, 17002 (2012).

[26] T. Urata, Y. Tanabe, K. K. Huynh, H. Oguro, K. Watanabe, S. Heguri, and K. Tanigaki, Phys. Rev. B **89**, 024503 (2014).

[27] R. Peng, H. C. Xu, S. Y. Tan, H. Y. Cao, M. Xia, X. P. Shen, Z. C. Huang, C. Wen, Q. Song, T. Zhang, B. P. Xie, X. G. Gong, and D. L. Feng, Nat. Commun. **5**, 5044 (2014).

[28] G. Phan *et al.*, Proceedings of the JPS Spring Meeting, 2014 (unpublished).

[29] K. Nakayama *et al.* (unpublished).

[30] Y. Yamakawa, S. Onari, and H. Kontani, Phys. Rev. B **87**, 195121 (2013).

[31] R. M. Fernandes, A. V. Chubukov, and J. Schmalian, Nat. Phys. **10**, 97 (2014).

[32] S. Onari and H. Kontani, Phys. Rev. Lett. **109**, 137001 (2012).

[33] A. E. Böhmer, F. Hardy, F. Eilers, D. Ernst, P. Adelmann, P. Schweiss, T. Wolf, and C. Meingast, Phys. Rev. B **87**, 180505 (2013).

[34] K. K. Huynh, Y. Tanabe, T. Urata, H. Oguro, S. Heguri, K. Watanabe, and K. Tanigaki, Phys. Rev. B **90**, 144516 (2014).

[35] Y. Mizuguchi, F. Tomioka, S. Tsuda, T. Yamaguchi, and Y. Takano, J. Phys. Soc. Jpn. **78**, 074712 (2009).

[36] T. Terashima, N. Kikugawa, A. Kiswandhi, E.-S. Choi, J. S. Brooks, S. Kasahara, T. Watashige, H. Ikeda, T. Shibauchi, Y. Matsuda, T. Wolf, A. E. Böhmer, F. Hardy, C. Meingast, H. v. Löhneysen, M.-T. Suzuki, R. Arita, and S. Uji, Phys. Rev. B **90**, 144517 (2014).

[37] M. D. Watson, T. Yamashita, S. Kasahara, W. Knafo, M. Nardone, J. Béard, F. Hardy, A. McCollam, A. Narayanan, S. F. Blake, T. Wolf, A. A. Haghighirad, C. Meingast, A. J. Schofield, H. v. Löhneysen, Y. Matsuda, A. I. Coldea, and T. Shibauchi, Phys. Rev. Lett. **115**, 027006 (2015).

[38] S. Margadonna, Y. Takabayashi, M. T. McDonald, K. Kasperkiewicz, Y. Mizuguchi, Y. Takano, A. N. Fitch, E. Suarde, and K. Prassides, Chem. Commun. (Cambridge) **43**, 5607 (2008).

[39] K. Nakamura, R. Arita, and H. Ikeda, Phys. Rev. B **83**, 144512 (2011).

[40] S. Mukherjee, A. Kreisel, P. J. Hirschfeld, and B. M. Andersen, Phys. Rev. Lett. **115**, 026402 (2015).

[41] J. Maletz, V. B. Zabolotnyy, D. V. Evtushinsky, S. Thirupathaiah, A. U. B. Wolter, L. Harnagea, A. N. Yaresko, A. N. Vasiliev, D. A. Chareev, A. E. Böhmer, F. Hardy, T. Wolf, C. Meingast, E. D. L. Rienks, B. Büchner, and S. V. Borisenko, Phys. Rev. B **89**, 220506 (2014).

[42] J. S. Kim, D. G. Seiler, and W. F. Tseng, J. Appl. Phys. **73**, 8324 (1993).

[43] T. Urata, Y. Tanabe, K. K. Huynh, S. Heguri, H. Oguro, K. Watanabe, and K. Tanigaki, Phys. Rev. B **91**, 174508 (2015).

[44] A. V. Chubukov, R. M. Fernandes, and J. Schmalian, Phys. Rev. B **91**, 201105 (2015).

[45] H. Hosono and K. Kuroki, Phys. C **514**, 399 (2015).

[46] T. Watashige, Y. Tsutsumi, T. Hanaguri, Y. Kohsaka, S. Kasahara, A. Furusaki, M. Sigrist, C. Meingast, T. Wolf, H. v. Lohneysen, T. Shibauchi, and Y. Matsuda, Phys. Rev. X **5**, 031022 (2015).

[47] J. K. Dong, T. Y. Guan, S. Y. Zhou, X. Qiu, L. Ding, C. Zhang, U. Patel, Z. L. Xiao, and S. Y. Li, Phys. Rev. B **80**, 024518 (2009).

[48] D. Liu, W. Zhang, D. Mou, J. He, Y.-B. Ou, Q.-Y. Wang, Z. Li, L. Wang, L. Zhao, S. He, Y. Peng, X. Liu, C. Chen, L. Yu, G. Liu, X. Dong, J. Zhang, C. Chen, Z. Xu, J. Hu, X. Chen, X. Ma, Q. Xue, and X. Zhou, Nat. Commun. **3**, 931 (2012).